nature photonics

ARTICLES

PUBLISHED ONLINE: 10 JULY 2011 | DOI: 10.1038/NPHOTON.2011.129

Zero phase delay in negative-refractive-index photonic crystal superlattices

S. Kocaman[1]*, M. S. Aras[1], P. Hsieh[1], J. F. McMillan[1], C. G. Biris[2], N. C. Panoiu[2], M. B. Yu[3], D. L. Kwong[3], A. Stein[4] and C. W. Wong[1]*

We show that optical beams propagating in path-averaged zero-index photonic crystal superlattices can have zero phase delay. The nanofabricated superlattices consist of alternating stacks of negative index photonic crystals and positive index homogeneous dielectric media, where the phase differences corresponding to consecutive primary unit cells are measured with integrated Mach-Zehnder interferometers. These measurements demonstrate that at path-averaged zero-index frequencies the phase accumulation remains constant and equal to zero despite the increase in the physical path length. We further demonstrate experimentally that these superlattice zero-$\bar{n}$ bandgaps remain invariant to geometrical changes of the photonic structure and have a center frequency which is deterministically tunable. The properties of the zero-$\bar{n}$ gap frequencies, optical phase, and effective refractive indices are well described by detailed experimental measurements, rigorous theoretical analysis, and comprehensive numerical simulations.

An intense degree of interest in negative-index metamaterials (NIMs)[1,2] has developed in recent years. Metal-based NIMs[3–11] have been actively studied because of their unusual physical properties and their potential for use in many technological applications[12–22]; however, they usually have the disadvantage of demonstrating large optical losses in their metallic components. As an alternative to metal-based NIMs, dielectric-based photonic crystals (PhCs) have been investigated and shown to emulate the basic physical properties of NIMs[23–27], while also having relatively small absorption losses at optical frequencies. Equally important, PhCs can be nanofabricated within current silicon foundries, suggesting significant potential for the development of future electronic–photonic integrated circuits.

One particular type of PhC can be obtained by cascading alternating layers of NIMs and positive-index materials (PIMs)[28–32]. This photonic structure (Fig. 1) has unique optical properties, including new surface states and gap solitons[33,34], unusual transmission and emission properties[35–39], complete photonic bandgaps[40], and a phase-invariant field for cloaking applications[41]. Moreover, these binary photonic structures have an omnidirectional bandgap that is insensitive to wave polarization, incidence angle, structure periodicity and structural disorder[42–44]. Such a gap exists because the path-averaged refractive index is equal to zero within a certain frequency band[28–32,35]. At this frequency, the Bragg condition, $k\Lambda = (\bar{n}\omega/c)\Lambda = m\pi$, is satisfied for $m = 0$, irrespective of the period Λ of the superlattice (k and ω are the wave vector and frequency, respectively, and $\bar{n}$ is the averaged refractive index). Because of this property this photonic bandgap is called zero-$\bar{n}$, or zero-order bandgap[30,35].

Near-zero-index materials have a series of exciting potential applications, such as beam self-collimation[35], extremely convergent lenses and spontaneous emission control[36], strong field enhancement[38] and cloaking devices[41]. The vanishingly small value of the refractive index of near-zero-index materials and their large phase velocity[19] can reshape electromagnetic phase fronts emitted by optical antennas[37] or, for highly directive antennas, transfer near-field phase information into the far-field. In the near-zero-index regime, the electromagnetic field has an unusual dual character; that is, it is static in the spatial domain (the phase difference between arbitrary spatial locations is equal to zero), while remaining dynamic in the time domain, thus allowing energy transport. Perhaps the most important application of near-zero-index materials is in optical links in lumped nanophotonic circuits[45]. In particular, chip-scale optical interconnects or interferometers that can guide light over hundreds of wavelengths without introducing phase variations can be effectively used to reduce the unwanted effects of frequency dispersion. This remarkable property, which is also the main topic of our study, has other exciting technological applications in photon delay lines with zero phase difference, information-processing devices, and new optical phase control and measurement techniques.

In this Article, we demonstrate the zero phase delay at near-infrared wavelengths in chip-scale photonic superlattices that consist of alternating PhC-based NIM and homogeneous slab waveguide PIM layers. First, we observe the existence of the zero-$\bar{n}$ gaps, a prerequisite for zero phase delays, and demonstrate the zero-$\bar{n}$ gap invariance to structural changes and their deterministically tunable centre frequency. Next, by embedding the negative–positive index binary superlattices in integrated Mach–Zehnder interferometers (MZIs), we describe a series of measurements where the total phase accumulation in the superlattice is equal to zero, at the path-averaged zero-index frequencies. Furthermore, we present comparative phase delay studies across different superlattice configurations and negative-index unit cells, and detailed numerical simulations that prove that these zero-$\bar{n}$ gaps are robust to effects induced by structural disorder.

Existence, invariance and tunability of zero-$\bar{n}$ gap

First, we examine zero-$\bar{n}$ superlattices and show experimentally that the zero-$\bar{n}$ gap markedly differs from a regular Bragg gap.

---

[1]Optical Nanostructures Laboratory, Center for Integrated Science and Engineering, Solid-State Science and Engineering, Mechanical Engineering, Columbia University, New York, New York 10027, USA, [2]Photonics Group, Department of Electronic and Electrical Engineering, University College London, Torrington Place, London WC1E 7JE, UK, [3]The Institute of Microelectronics, 11 Science Park Road, Singapore Science Park II, Singapore 117685, Singapore, [4]Center for Functional Nanomaterials, Brookhaven National Laboratory, Upton, New York 11973, USA. *e-mail: sk2927@columbia.edu; cww2104@columbia.edu

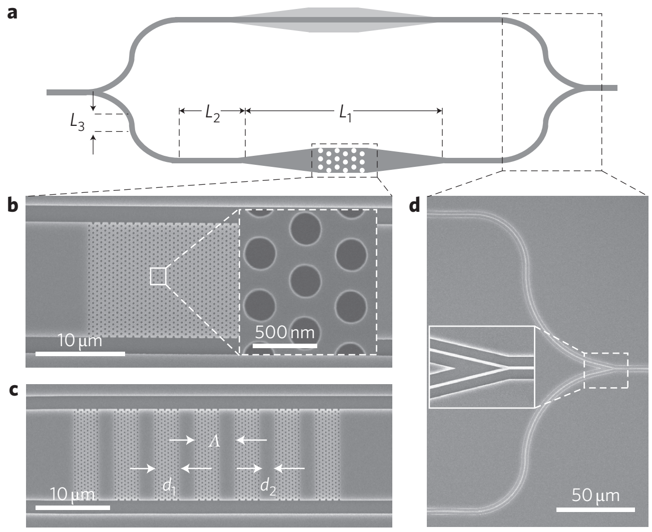

Figure 1 | Schematic of an MZI and scanning electron microscopy (SEM) images of the fabricated device. **a**, Schematic representation of the MZI ($L_1 \approx 850$ μm; $L_2 \approx 250$ μm; L_3 is initially zero and is incremented by additional SPs in the phase measurements). **b**, SEM image of a sample, showing the PhC layer only (period of hexagonal lattice, $a = 423$ nm; ratio between hole radius and period, $r/a = 0.283$; ratio between thickness of wafer and period, $t/a = 0.756$). Inset: zoomed-in image. (For a schematic representation of the PhC and superlattice, see Supplementary Fig. S1.) **c**, SEM image of a fabricated superlattice with seven SPs. Each PhC layer contains seven unit cells of PhCs ($d_1 = 2.564$ μm, $d_2 = 2$ μm, $\Lambda = 4.564$ μm) with the same parameters as in **b**. **d**, SEM image of the Y-branch. Inset: zoomed-in image.

In particular, because this gap is formed when the spatially averaged index is zero, it is insensitive to superlattice period variations as long as the condition of zero average index is satisfied[28–32,35]. This property also implies that the total phase accumulation upon beam propagation in the superlattice cancels at wavelengths corresponding to the zero-$\bar{n}$ gap.

The existence of zero-$\bar{n}$ bandgaps can be inferred from the Bloch–Floquet theorem, where for a one-dimensional (1D) binary periodic lattice the trace of the transfer matrix, T, of a primary unit cell can be expressed as[28,30]

$$Tr[T(\omega)] = 2\cos(\kappa\Lambda) = 2\cos\left(\frac{\bar{n}\omega\Lambda}{c}\right) - \left(\frac{Z_1}{Z_2} + \frac{Z_2}{Z_1} - 2\right) \times \sin\left(\frac{n_1\omega d_1}{c}\right)\sin\left(\frac{n_2\omega d_2}{c}\right) \tag{1}$$

where $n_{1(2)}$ and $Z_{1(2)}$ are the refractive index and impedance of the first (second) layer, respectively, and κ is the Bloch wave vector of the electromagnetic mode. Equation (1) implies that if the spatially averaged refractive index is zero ($\bar{n} = 0$), all solutions for the wave vector are imaginary, which signifies the presence of a spectral bandgap[28–31].

The photonic structures examined for zero-$\bar{n}$ gaps (Fig. 1) consist of dielectric PhC superlattices with alternating layers of negative-index PhC and positive-index homogeneous slabs[30]. The PhC band structure is shown in Fig. 2a,b, with geometrical parameters from averaged fabricated samples (hole-to-lattice constant (r/a) ratio of 0.283 and $a \approx 423$ nm). This two-dimensional (2D) hexagonal PhC has a negative index within the spectral band of 0.270–0.278, in normalized frequencies of $\omega a/2\pi c$, or wavelengths from 1,520 nm to 1,566 nm. The phase index of refraction is defined with respect to the wave vector in the first Brillouin zone, as described in refs 27 and 46. Although alternative choices can be used, such as the wave vector of the plane wave with the largest amplitude in the Fourier series decomposition of the Bloch mode[47], our approach provides a convenient method with which to analyse the phase properties of the optical modes of the PhC. In our design, the longitudinal direction of the superlattice (z-axis) coincides with the Γ–M axis of the hexagonal PhC. The 1D binary superlattice and the hexagonal PhC have different symmetry properties and therefore different first Brillouin zones (Supplementary Fig. S1). Moreover, within our operating wavelength range (Fig. 2b) the PhC has two transverse-magnetic (TM)-like bands, one with a positive refractive index and the other with a negative refractive index, and an almost complete transverse-electric (TE)-like bandgap.

We fabricated a set of three devices of different periods Λ, with the negative-index PhC layer in the superlattice spanning 7, 9 and 11 unit cells along the z-axis, so that the thickness of this layer was $d_1 = 3.5\sqrt{3}\ a$ (2.564 μm), $d_1 = 4.5\sqrt{3}\ a$ (3.297 μm) and $d_1 = 5.5\sqrt{3}\ a$ (4.029 μm), respectively. Our experiments spanned 1,520 nm to 1,620 nm, with the negative refractive index band existing for wavelengths up to 1,570 nm. The effective refractive index of the PhC region was obtained from the band diagram (Fig. 2a,b, see Methods) and the PIM layer index computed from the asymmetric TM slab-waveguide mode effective index (for example, at 1,550 nm the mode index is 2.671). To locate the zero-$\bar{n}$ frequency in the middle of our negative-index band, the length ratio between the PIM and PhC sections of the superlattice was set to 0.78. As such, the zero-$\bar{n}$ gap should occur at 1,552.6 nm (see Supplementary Information). The corresponding PIM layer thickness was determined by requiring the average index to be zero [$\bar{n} = (n_1 d_1 + n_2 d_2)/\Lambda = 0$], while keeping the ratio d_2/d_1 unchanged for all three devices in the set. Here, n_1 and n_2 are the effective mode indices in the PhC and homogeneous layers, respectively, at the corresponding wavelengths. This leads to the following values for the superperiods (SPs): $\Lambda_{7\mathrm{UC}} = 4.564$ μm, $\Lambda_{9\mathrm{UC}} = 5.869$ μm and $\Lambda_{11\mathrm{UC}} = 7.173$ μm. Example transmission spectra for the fabricated samples are summarized in Fig. 2c, and show that the zero-$\bar{n}$ gap is $\sim$1,557.8 ± 1.5 nm, very close to the theoretically predicted values ($\Delta\lambda/\lambda < 0.5\%$) and numerically computed spectra. In the Supplementary Information, we further demonstrate the tunability of the zero-$\bar{n}$ gap and provide near-field scanning optical microscope images to confirm transmission.

MZ interference with negative-refraction PhCs on both arms

We next examine PhC structures integrated with MZIs for phase-delay measurements. In most free-space interferometric applications, the phase difference leading to interference originates from the physical length difference between the two arms, but in integrated photonic circuits this delay can easily be modulated by the imbalance in the refractive indices of two arms (see Supplementary Information and ref. 48). As illustrated in Fig. 1a, the unbalanced interferometer is designed so that after splitting from the Y-branch (Fig. 1d); a single-mode input channel waveguide adiabatically tapers (over $\sim$400 μm) to match the width of the superlattice structures. On the reference arm, there is either a slab (with or without PhC) that has the geometry required to match the index variations in the other arm and hence isolate the additional phase contribution of the PhC structures, or a channel waveguide leading to a large index difference and hence to distinctive Mach–Zehnder fringes.

For this purpose, we designed and fabricated 100 unit cells of PhC on one arm of the MZI and a geometrically identical homogeneous slab on the other arm (see Methods). In the transmission (Fig. 3b; red), the MZ interference spectra are slowly varying as expected, due to small imbalance in the MZI. However, there are two steep variations, the first at the end of the

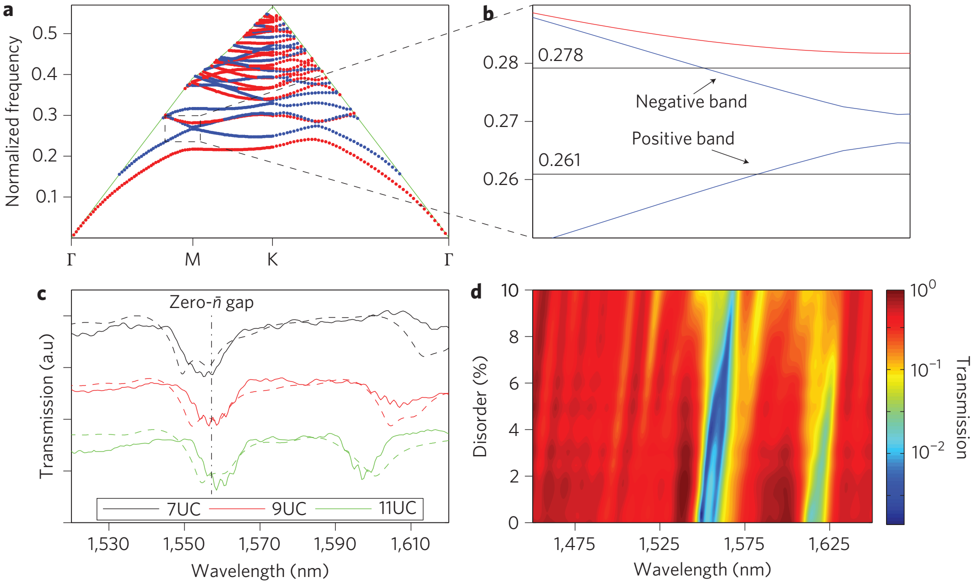

Figure 2 | Band diagram of the PhC, verification of period-invariant zero-$\bar{n}$ bandgaps, and influence of structural variations on transmission spectra. a, Band diagram of the PhC with the parameters given in Fig. 1 (for a schematic of the Brillouin zones, see Supplementary Fig. S1). The TM-like and TE-like photonic bands are depicted in blue and red, respectively. The light cone is denoted by green lines. **b**, A zoomed-in representation of the spectral domain corresponding to the experimental region of interest. Experiments were performed in the spectral region delineated by two horizontal lines (normalized frequency, 0.278–0.261). **c**, Experimental verification of the zero-$\bar{n}$ bandgap in superlattices with varying period ($\Lambda_{\text{black}} = 4.56$ μm, $\Lambda_{\text{red}} = 5.87$ μm and $\Lambda_{\text{green}} = 7.17$ μm) and the same ratio $d_2/d_1 = 0.78$ (a.u., arbitrary units), and numerically simulated transmission spectra (dashed lines). **d**, Influence of lattice disorder (parameter σ) on transmission spectra. Colour bar: transmission scaling.

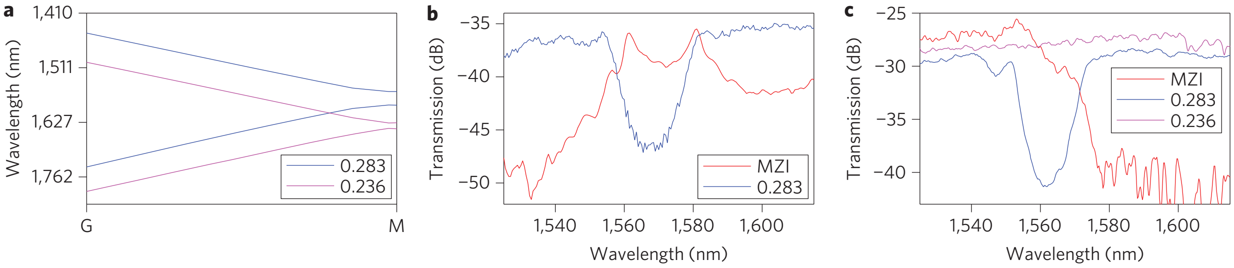

Figure 3 | MZ interferences with negative refraction PhCs. a, The band diagram shifts to lower frequency when the r/a ratio changes. Blue, original design; purple, design with $r/a = 0.236$. **b**, Red line: MZI transmission with 100 unit cells of PhC on one arm and a homogeneous slab waveguide on the other arm. Blue line: transmission spectrum for non-MZI PhC with 60 PhC unit cells. **c**, Red line: MZI transmission with 62 unit cells of PhC on one arm with $r/a = 0.283$ and 62 unit cells of PhC with $r/a = 0.236$ on the other arm; lattice period a is the same in both cases. Blue line: transmission spectrum for PhC superlattice with $r/a = 0.283$ and 80 unit cells of PhC. Purple line: transmission spectrum for PhC superlattice with $r/a = 0.236$ and 80 unit cells of PhC. Different index differences Δn from 1,525 nm to 1,550 nm and from 1,580 nm to 1,615 nm give different phase difference ϕ and different interference output.

first (negative-index) band and the second at the start of the second (positive-index) band. This is a clear indication of an abrupt refractive index change (Supplementary Fig. S2c), which is only possible when there is an abrupt switch between two photonic bands (a band-to-band transition). A non-MZI transmission spectrum of a similar structure is shown in Fig. 3b (blue) for reference.

To characterize this steep index change further, we placed on the two arms of the MZI PhC, sections of different radius r. We kept a unchanged to retain the same total physical length on both arms, for the same number of unit cells in the PhC sections. With this approach, the MZI sections that do not contain PhC regions are identical, so the two PhC sections are the only source for any measured phase difference. For example, we set r_2 to 5/6 of the original value of the radius r_1 ($r_2/a = 0.283 \times 5/6 = 0.236$). Figure 3a illustrates the difference between the band structures of the two PhC designs, namely, a frequency shift of the photonic bands. As a result of this shifted band structure, the accumulated phase difference between the two arms is almost independent of wavelength, except for a steep variation that again corresponds to a steep refractive index change (moving from band to band). When we place a section of 62 PhC unit cells in both arms of the MZI, the transmission spectra have two spectral domains, 1,525–1,550 nm and 1,580–1,615 nm, where the interference transmission is rather constant (red curve in Fig. 3c) with ~14 dB transmission difference between the two domains (for high spatial resolution images, see Supplementary Fig. S6).

MZ phase delay measurements with photonic superlattices

Next, we prove that the total phase accumulation in the superlattices is zero. In these measurements we used a single-mode channel waveguide for the MZI reference arm. Owing to the large imbalance between the tapering slab and the channel waveguide, a series of high-visibility interference fringes can be observed at the output

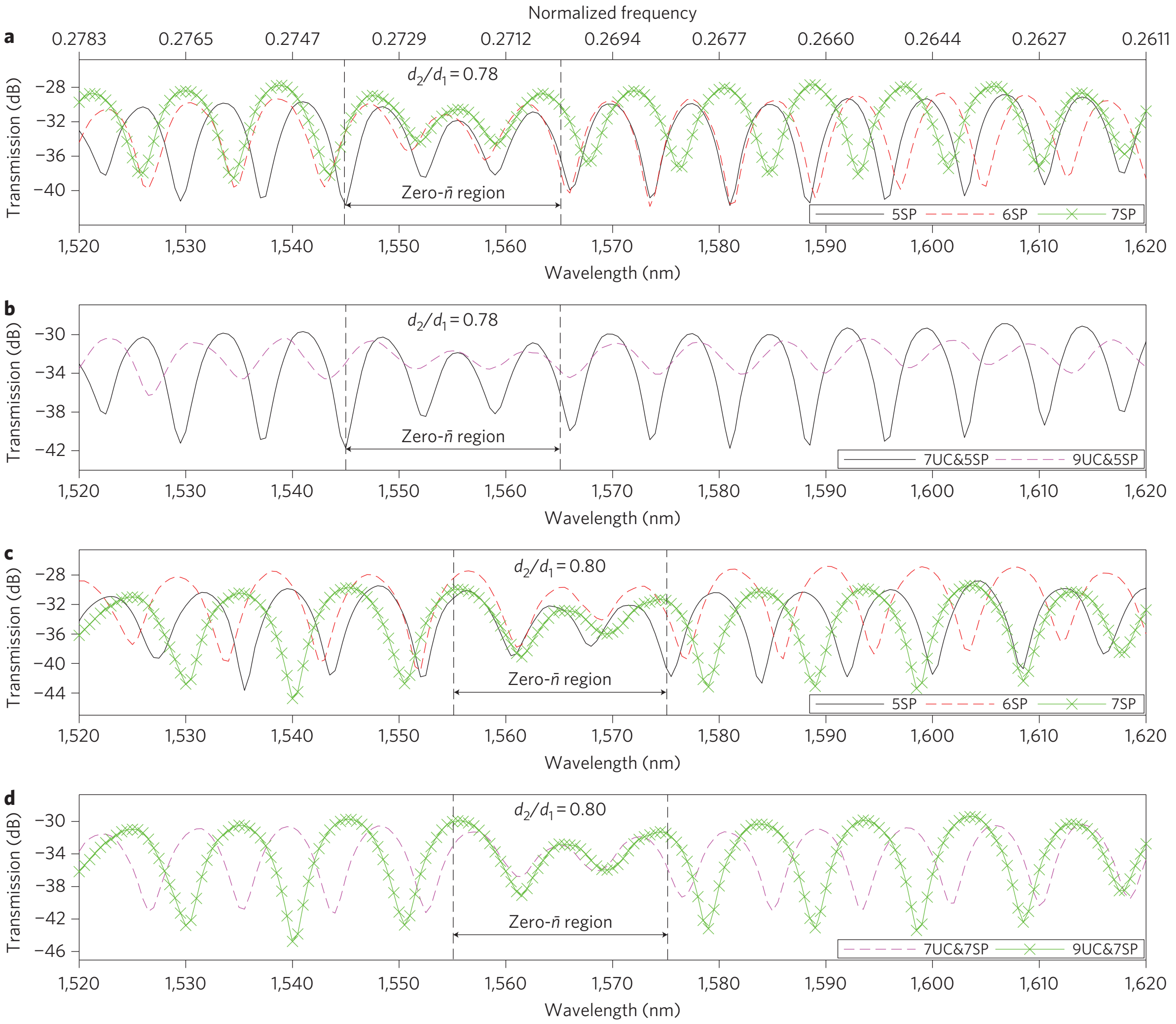

Figure 4 | Phase measurements. a, Output of the MZI with increasing number of SPs (5, 6 and 7) on one arm and single-mode channel waveguides on the other. Each PhC layer contains seven unit cells ($d_1 = 2.564$ μm, $d_2 = 2$, $d_2/d_1 = 0.78$ and $\Lambda = 4.564$ μm). **b**, As in **a**, with increasing number of unit cells in each SP (7UC, $\Lambda = 4.564$ μm; 9UC, $\Lambda = 5.869$ μm); each device has five SPs. **c**, As in **a**, but for $d_2/d_1 = 0.8$ and nine unit cells in each PhC layer ($d_1 = 3.297$ μm, $d_2 = 2.572$, $d_2/d_1 = 0.78$, $\Lambda = 5.869$ μm). **d**, As in **b**, with $d_2/d_1 = 0.8$ (7UC, $\Lambda = 4.616$ μm; 9UC, $\Lambda = 5.935$ μm); each device has seven SPs.

and used to determine the phase delay by analysing the fringe spectral locations and peak-to-peak free spectral range (FSR). We designed the taper length to have a large number of fringes within the measurement window. With this approach we avoid the uncertainty of transmission and coupling losses (and the resulting normalization by the individual device transmissions) when determining the phase differences between devices. We performed phase measurements for four different sets of devices: (i) $d_2/d_1 = 0.78$ and seven unit cells in the PhC layer, with increasing number of SPs (5, 6 and 7); (ii) $d_2/d_1 = 0.78$ and five SPs with different unit cells in the PhC layers (7 and 9); (iii) $d_2/d_1 = 0.80$ and nine unit cells in the PhC layer with increasing number of SPs (5, 6 and 7); and (iv) $d_2/d_1 = 0.80$ and seven SPs with different unit cells in the PhC layers (7 and 9). When we designed these devices, we modified the MZI so that when we added a SP to the superlattice the length of the adiabatic transition arms was increased by $\Lambda/2$, making the horizontal single-mode channel waveguides shorter (from L_2 to $L_2 - \Lambda/2$), at both the input and output sides of the device arm in Fig. 1a (for a schematic illustration, see Supplementary Fig.S3). This change is compensated by adding the same length to the vertical part (from L_3 to $L_3 + \Lambda/2$ on both sides in Fig. 1a). As a result, the only phase difference between devices is due to the additional SPs. At each wavelength, the phase difference between the waves propagating in the two arms of the MZI is given by (see Supplementary Information)

$$\cos[\phi] = \cos\left[\frac{2\pi}{\lambda}\left(\left(n_{\mathrm{slab}} - n_{\mathrm{wg}}\right)L_{\mathrm{slab}} + n_{\mathrm{sl}}L_{\mathrm{sl}}\right)\right] \qquad (2)$$

where n_{slab}, n_{wg} and n_{sl} are the refractive indices of the tapering slab, the channel waveguide and the superlattice, respectively. These have different frequency dispersions, and therefore different functional dependence on the probed wavelength. L_{sl} and L_{slab} are the physical lengths of the superlattice and the tapering slab (total ~850 μm). Figure 4a shows the interference pattern for $d_2/d_1 = 0.78$ with seven unit cells in the PhC layer. As shown, outside the zero-$\bar{n}$ spectral region the fringes differ from each other both in wavelength and FSR, but overlap very well within the zero-$\bar{n}$ spectral domain, indicating that the additional phase contribution from the $n_{\mathrm{sl}}L_{\mathrm{sl}}$ term in equation (2) is zero.

To further illustrate the phase evolution, we show in Fig. 5a the FSR values for each of the devices examined — specifically, we calculate the spectral spacing between the transmission minima and plot the spectral spacing versus centre wavelength between the two

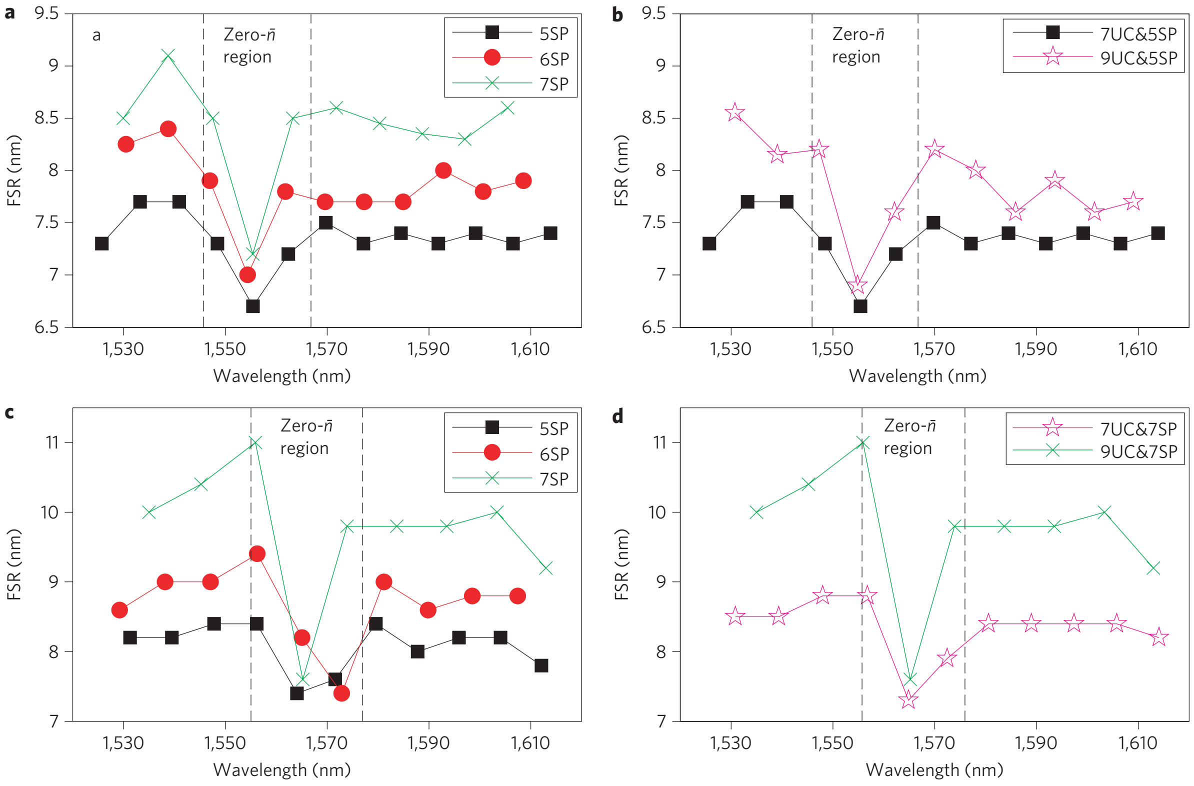

Figure 5 | FSR wavelength dependence corresponding to superlattices in Fig. 4. a–d, FSR spectral spacing between the transmission minima versus centre wavelength between the two neighbouring minima, extracted from the data in Fig. 4a–d. At the zero-$\bar{n}$ bandgap wavelength, the FSR does not change between devices when the physical length of the MZI arm increases, which proves the zero phase contribution from the added SPs.

neighbouring minima. As noted above, in general there is an inherent FSR due to the MZI imbalance, and after adding each SP the FSR increases, so the imbalance decreases. However, in the zero-$\bar{n}$ spectral domain the FSR corresponding to each of the devices approaches the same value, indicating that the corresponding phase difference remains constant. This is a surprising conclusion, because the physical path is certainly not the same in all cases. This apparent paradox has a simple explanation: although the physical path difference varies among the three cases the corresponding optical path difference is the same as the spatially averaged refractive index of the three superlattices vanishes. In other words, within the zero-$\bar{n}$ spectral region the photonic superlattice emulates the properties of a zero phase delay line.

The output corresponding to the structures with $d_2/d_1 = 0.78$ and five SPs with different unit cells (7 and 9) in the PhC layer is shown in Fig. 4b, and the FSR values are plotted in Fig. 5b. Here, the device with seven unit cells is the same as the one corresponding to the results in Fig. 4a. Remarkably, although the additional length is different in this case (instead of a length difference of $2 \times \Lambda_{7\mathrm{UC}}$, we have now added a length of $5 \times (\Lambda_{9\mathrm{UC}} - \Lambda_{7\mathrm{UC}})$), we again obtain a good overlap in the interference pattern and a match in the FSR value. Therefore, the phase difference is independent of the length of the superlattice (see also equation 2); this further proves that we indeed observe a zero phase difference and not a multiple of 2π. In other words, if $\bar{n} \times \Lambda_{7\mathrm{UC}}$ ($\bar{n} \times 4.56$ μm) and $\bar{n} \times \Lambda_{9\mathrm{UC}}$ ($\bar{n} \times 5.87$ μm) are multiples of $\lambda/2$ at $\lambda = 1{,}557.8$ nm, the only possible solution is that the multiple is equal to zero. With this, we also prove a fundamental difference between a Bragg gap and the zero-$\bar{n}$ gap; the former scales with the lattice period Λ and forms at multiples of 2π, whereas the latter is independent of Λ and occurs at a constant wavelength as long as the property of path-averaged zero index is preserved.

Finally, Fig. 4c,d and Fig. 5c,d show the interference patterns for the case of $d_2/d_1 = 0.80$ and nine unit cells in the PhC layer with increasing number of SPs (5, 6 and 7) and with seven SPs with changing number of unit cells in the PhC layer (7 and 9), respectively. Again, both the FSR (Fig. 5c,d) and absolute wavelength values (Fig. 4c,d) overlap in the zero-$\bar{n}$ spectral domain, proving the zero phase variation across the superlattices.

Robustness against structural disorder

One of the main properties of zero-$\bar{n}$ bandgaps is their remarkable robustness against effects induced by structural disorder. To study this property, we considered the optical transmission in randomly perturbed photonic superlattices. Specifically we considered superlattices for which the PIM lengths were randomly distributed within the domain ($d_2 - \Delta d_2/2$, $d_2 + \Delta d_2/2$), amounting to a random variation of SP Λ. The degree of structural disorder is quantified by the parameter $\sigma = \Delta d_2/d_2$. The main results of our computational investigation are presented in Fig. 2d. It can be clearly seen that the zero-$\bar{n}$ bandgap is preserved, even when the disorder parameter is as large as $\sigma = 10\%$, that is, a value much larger than arising from our fabrication processes. Note that the amplitude oscillations in the transmission spectra represent Fabry–Perot resonances in the superlattice. In addition, our numerical simulations show that the structural disorder associated with a random perturbation of the hole radii or their location has a comparable or smaller influence on the existence of zero-$\bar{n}$ bandgaps (Supplementary Fig. S7a,b).

Conclusion

We have demonstrated, for the first time, zero phase delay in negative–positive-index superlattices, in addition to observations of deterministic zero-$\bar{n}$ gaps that remain invariant to geometric changes. Through stable chip-scale interferometric measurements, binary superlattices of varying lengths are shown unequivocally to enable rigorous control of the optical phase. Devices with different SPs, unit cells and negative–positive length ratios have all demonstrated the presence of the zero phase delay. Engineered control of the phase delay in these near-zero refractive index superlattices can be implemented in chip-scale transmission lines and interferometers with deterministic phase array and dispersion control, and has significant technological potential in phase-insensitive image processing, phase-invariant fields for electromagnetic cloaking, lumped elements in optoelectronics, information processing, and engineering of radiation wavefronts to pre-designed shapes.

Methods

Numerical simulations. The band diagram in Fig. 2a was calculated using RSoft's BandSOLVE, a commercially available software that implements a numerical method based on the plane wave expansion of the electromagnetic field. Three-dimensional simulations were performed to calculate 30 bands. In all these numerical simulations, a convergence tolerance of 1×10^{-8} was used. The photonic bands were divided into TM-like and TE-like, according to their parity symmetry. The path-averaged index of the superlattice was calculated using the negative effective index of the second TM-like band and the effective modal index of the homogeneous asymmetric slab waveguide.

The effective refractive indices corresponding to the TM-like bands (Fig. 2b) were determined from the relation $k = \omega|n|/c$ (with k in the first Brillouin zone) (see Supplementary Information). Note that, for the second band, the effective index of refraction is negative because k decreases with ω (ref. 23).

The transmission spectra were determined using MIT's MEEP[49], a freely available code based on the finite-difference time-domain (FDTD) method. In all numerical simulations we used a uniform computational grid of 40 grid points per micrometre. This ensured that a widely used rule-of-thumb for setting the size of the computational grid in FDTD simulations was satisfied, namely, that the smallest characteristic length of the system (in our case, the diameter of the holes) contained at least 10 grid points. The transmission spectra corresponding to a specific geometry of the photonic superlattice were determined by normalizing the transmission spectrum of the photonic superlattice to the transmission spectrum of the homogeneous structure that was obtained by replacing the PhC regions with homogeneous slabs. In all our FDTD-based numerical simulations we used a pulsed excitation source with a central wavelength of $\lambda_0 = 1{,}550$ nm and spectral full-width at half-maximum of 90 nm. A typical simulation run on 64 Intel®Xeon processors was performed in ~7 h.

Sample nanofabrication. The PhC structures shown in Fig. 1 were fabricated as a hexagonal lattice of air holes arranged on a silicon on insulator (SOI) wafer with a 320 nm-thick silicon slab ($n_{\mathrm{Si}} = 3.48$) on top of a 2-μm-thick layer of buried oxide ($n_{\mathrm{SiO2}} = 1.46$), either with electron-beam or deep-UV lithography. For electron-beam lithography, ZEP520A (100%) positive tone electron-beam resist was spin-coated at 4,000 r.p.m. to a thickness of 370 nm, and baked at 180 °C for 3 min. A JEOL JBX6300FS electron-beam lithography system was used to expose the pattern, followed by development in amyl acetate for 90 s, and rinsing with isopropyl alcohol (IPA) for 45 s to completely remove the developer (amyl acetate) residue.

For pattern transferring into silicon, an Oxford instruments Plasmalab 100 was used to perform cryogenic etching of the silicon[50] using an inductively coupled plasma reactive ion etcher (ICP-RIE). First, we applied 10 min O_2 cleaning at –100 °C in the chamber, followed by cryogenic etching at –100 °C using a mixture of SF_6 (40 s.c.c.m) and O_2 (18 s.c.c.m.) at 15 W radiofrequency (rf) power, 800 W ICP power and 12 mtorr pressure for a total of 18 s. Subsequently, the wafer was placed in 1165 resist remover for ~4 h to completely remove the remainder of the resist. The chip was cleaved and mounted on the sample holder for measurements.

Experiments. An in-line fibre polarizer with a polarization controller was used to couple TE light from an amplified spontaneous emissions source (ranging from 1,520 nm to 1,620 nm) into the waveguide via a tapered lensed fibre. A second tapered lensed fibre collected the transmission from the waveguide output, and the signal was sent to an optical spectrum analyser (OSA).

It should be noted that in all our plots of experimental data we used raw data, so there was no data post-processing, except for intensity rescaling. Measurements were taken three times with 500 pm resolution for Figs 2c and 3b,c, 100 pm and 500 pm resolutions for Fig. 4a, and 200 pm and 500 pm resolutions for Fig. 4b–d. There is ~0.5% deviation between Fig. 3b and Fig. 3c in terms of the centre frequency of the bandgap region, because of fabrication differences between the samples. In Figs 2c, 4 and 5, the r/a ratio was <5% smaller than in Fig, 3b, resulting in a shift of the band structure to lower frequencies (but in Fig. 3c was <5% larger than in Fig. 3b, leading to a shift of the band structure to higher frequencies), consequently causing a shift of the zero-$\bar{n}$ bandgap.

For the three devices in Fig. 2c, we designed seven SPs for the devices with seven unit cells of PhC, and five SPs for those with nine and eleven unit cells of PhC, to ensure a sufficient signal-to-noise ratio for the transmission measurements.

Received 28 November 2010; accepted 26 May 2011;

References

1. Veselago, V. G. The electrodynamics of substances with simultaneously negative values of ε and μ. *Usp. Fiz. Nauk* **92,** 517–526 (1964) [*Sov. Phys. Usp.* **10,** 509–514 (1968)].
2. Pendry, J. B. Time reversal and negative refraction. *Science* **322,** 71–73 (2008).
3. Shelby, R. A., Smith, D. R. & Schultz, S. Experimental verification of a negative index of refraction. *Science* **292,** 77–79 (2001).
4. Valentine, J. *et al.* Three-dimensional optical metamaterial with a negative refractive index. *Nature* **455,** 376–379 (2008).
5. Li, N. *et al.* Three-dimensional photonic metamaterials at optical frequencies. *Nat. Mater.* **7,** 31–37 (2008).
6. Gramotnev, D. K. & Bozhevolnyi, S. I. Plasmonics beyond the diffraction limit. *Nature Photon.* **4,** 83–91 (2010).
7. Shalaev, V. M. Optical negative-index metamaterials. *Nature Photon.* **1,** 41–48 (2007).
8. Kundtz, N. & Smith, D. R. Extreme-angle broadband metamaterial lens. *Nat. Mater.* **9,** 129–132 (2010).
9. Panoiu, N. C. & Osgood, R. M. Influence of the dispersive properties of metals on the transmission characteristics of left-handed materials. *Phys. Rev. E* **68,** 016611 (2003).
10. Zhang, S. *et al.* Demonstration of near-infrared negative-index metamaterials. *Phys. Rev. Lett.* **95,** 137404 (2005).
11. Liu, R. *et al.* Experimental demonstration of electromagnetic tunneling through an epsilon-near-zero metamaterial at microwave frequencies. *Phys. Rev. Lett.* **100,** 023903 (2008).
12. Tsakmakidis, K. L., Boardman, A. D. & Hess, O. 'Trapped rainbow' storage of light in metamaterials. *Nature* **450,** 397–401 (2007).
13. Yao, J. *et al.* Optical negative refraction in bulk metamaterials of nanowires. *Science* **321,** 930 (2008).
14. Xi, S. *et al.* Experimental verification of reversed Cherenkov Radiation in left-handed metamaterial. *Phys. Rev. Lett.* **103,** 194801 (2009).
15. Hoffman, A. J. *et al.* Negative refraction in semiconductor metamaterials. *Nat. Mater.* **6,** 946–950 (2007).
16. Grigorenko, A. N. *et al.* Nanofabricated media with negative permeability at visible frequencies. *Nature* **438,** 335–338 (2005).
17. Dolling, G., Enkrich, C., Wegener, M., Soukoulis, C. M. & Linden, S. Simultaneous negative phase and group velocity of light in a metamaterials. *Science* **312,** 892–894 (2006).
18. Pollard, R. J. *et al.* Optical nonlocalities and additional waves in epsilon-near-zero metamaterials. *Phys. Rev. Lett.* **102,** 127405 (2009).
19. Ye, D., Qiao, S., Huangfu, J. & Ran, L. Experimental characterization of the dispersive behavior in a uniaxial metamaterial around plasma frequency. *Opt. Express* **18,** 22631–22636 (2010).
20. Jin, Y., Zhang, P. & He, S. Squeezing electromagnetic energy with a dielectric split ring inside a permeability-near-zero metamaterial. *Phys. Rev. B* **81,** 085117 (2010).
21. Hsueh, W. J., Chen, C. T. & Chen, C. H. Omnidirectional band gap in Fibonacci photonic crystals with metamaterials using a band-edge formalism. *Phys. Rev. A* **78,** 013836 (2008).
22. Xu, J.-P., Yang, Y.-P., Chen, H. & Zhu, S.-Y. Spontaneous decay process of a two-level atom embedded in a one-dimensional structure containing left-handed material. *Phys. Rev. A* **76,** 063813 (2007).
23. Chatterjee, R. *et al.* Achieving subdiffraction imaging through bound surface states in negative-refraction photonic crystals in the near-infrared range. *Phys. Rev. Lett.* **100,** 187401 (2008).
24. Decoopman, T., Tayeb, G., Enoch, S., Maystre, D. & Gralak, B. Photonic crystal lens: from negative refraction and negative index to negative permittivity and permeability. *Phys. Rev. Lett.* **97,** 073905 (2006).
25. Lu, Z. *et al.* Three-dimensional subwavelength imaging by a photonic-crystal flat lens using negative refraction at microwave frequencies. *Phys. Rev. Lett.* **95,** 153901 (2005).
26. Parimi, P. V., Lu, W. T., Vodo, P. & Sridhar, S. Photonic crystals: imaging by flat lens using negative refraction. *Nature* **426,** 404 (2003).
27. Notomi, M. Theory of light propagation in strongly modulated photonic crystals: Refractionlike behavior in the vicinity of the photonic band gap. *Phys. Rev. B* **62,** 010696 (2000).
28. Li, J., Zhou, L., Chan, C. T. & Sheng, P. Photonic band gap from a stack of positive and negative index materials. *Phys. Rev. Lett.* **90,** 083901 (2003).
29. Panoiu, N. C., Osgood, R. M., Zhang, S. & Brueck, S. R. J. Zero-*n* bandgap in photonic crystal superlattices. *J. Opt. Soc. Am. B* **23,** 506–513 (2006).
30. Kocaman, S. *et al.* Observations of zero-order bandgaps in negative-index photonic crystal superlattices at the near-infrared. *Phys. Rev. Lett.* **102,** 203905 (2009).
31. Yuan, Y. *et al.* Experimental verification of zero order bandgap in a layered stack of left-handed and right-handed materials. *Opt. Express* **14,** 2220–2227 (2006).

32. Zhang, L., Zhang, Y., He, L., Li, H. & Chen, H. Experimental investigation on zero-n_{eff} gaps of photonic crystals containing single-negative materials. *Eur. Phys. J. B* **62,** 1–6 (2008).
33. Hegde, R. S. & Winful, H. G. Zero-*n* gap soliton. *Opt. Lett.* **30,** 1852–1854 (2005).
34. Namdar, A., Shadrivov, I. V. & Kivshar, Y. S. Excitation of backward Tamm states at an interface between a periodic photonic crystal and a left-handed metamaterial. *Phys. Rev. A* **75,** 053812 (2007).
35. Mocella, V. *et al.* Self-collimation of light over millimeter-scale distance in a quasi-zero-average-index metamaterial. *Phys. Rev. Lett.* **102,** 133902 (2009).
36. Enoch, S., Tayeb, G., Sabouroux, P., Guérin, N. & Vincent, P. A metamaterial for directive emission. *Phys. Rev. Lett.* **89,** 213902 (2002).
37. Ziolkowski, R. W. Propagation in and scattering from a matched metamaterial having a zero index of refraction. *Phys. Rev. E* **70,** 046608 (2004).
38. Litchinitser, N. M., Maimistov, A. I., Gabitov, I. R., Sagdeev, R. Z. & Shalaev, V. M. Metamaterials: electromagnetic enhancement at zero-index transition. *Opt. Lett.* **33,** 2350–2352 (2008).
39. Wang, L-G., Li, G-X. & Zhu, S-Y. Thermal emission from layered structures containing a negative-zero-positive index metamaterial. *Phys. Rev. B* **81,** 073105 (2010).
40. Shadrivov, I. V., Sukhorukov, A. A. & Kivshar, Y. S. Complete band gaps in one-dimensional left-handed periodic structures. *Phys. Rev. Lett* **95,** 193903 (2005).
41. Hao, J., Yan, W. & Qiu, M. Super-reflection and cloaking based on zero index metamaterial. *Appl. Phys. Lett.* **96,** 101109 (2010).
42. Jiang, H., Chen, H., Li, H., Zhang, Y. & Zhu, S. Omnidirectional gap and defect mode of one-dimensional photonic crystals containing negative-index materials. *Appl. Phys. Lett.* **83,** 5386 (2003).
43. Bria, D. *et al.* Band structure and omnidirectional photonic band gap in lamellar structures with left-handed materials. *Phys. Rev. E* **69,** 066613 (2004).
44. Davoyan, A. R., Shadrivov, I. V., Sukhorukov, A. A. & Kivshar, Y. S. Bloch oscillations in chirped layered structures with metamaterials. *Opt. Express* **16,** 3299–3304 (2008).
45. Engheta, N. Circuits with light at nanoscales: optical nanocircuits inspired by metamaterials. *Science* **317,** 1698–1702 (2007).
46. Foteinopoulou, S. & Soukoulis, C. M. Electromagnetic wave propagation in two-dimensional photonic crystals: a study of anomalous refractive effects. *Phys. Rev. B* **72,** 165112 (2005).
47. Yariv, A. & Yeh, P. *Optical Waves in Crystals: Propagation and Control of Laser Radiation* (Wiley, 1984).
48. Vlasov, Y. A., O'Boyle, M., Hamann, H. F. & McNab, S. J. Active control of slow light on a chip with photonic crystal waveguides. *Nature* **438,** 65–69 (2005).
49. Oskooi, A. F. *et al.* MEEP: a flexible free-software package for electromagnetic simulations by the FDTD method. *Comp. Phys. Commun.* **181,** 687–702 (2010).
50. Henry, M. D., Welch, C. & Scherer, A. Techniques of cryogenic reactive ion etching in silicon for fabrication of sensors. *J. Vac. Sci. Technol. A* **27,** 1211–1216 (2009).

Acknowledgements

The authors thank R. Chatterjee for helpful discussions and Ayse Selin Kocaman for the preparation of figures. The authors also acknowledge funding support from a NSF CAREER Award (0747787), NSF ECCS (1102257), DARPA InPho and the EPSRC (EP/G030502/1). Electron-beam nanopatterning was carried out at the Center for Functional Nanomaterials, Brookhaven National Laboratory, which is supported by the US Department of Energy, Office of Basic Energy Sciences (contract no. DE-AC02-98CH10886). The authors acknowledge the use of the UCL Legion High Performance Computing Facility and associated support services in the completion of this work.

Author contributions

S.K. performed the experiments. M.S.A., M.B.Y., D.L.K. and A.S. nanofabricated the samples. P.H. performed near-field measurements. S.K., J.F.M., C.G.B. and N.C.P. designed and performed the numerical simulations. S.K., N.C.P. and C.W.W. prepared the manuscript.

Additional information

The authors declare no competing financial interests. Supplementary information accompanies this paper at www.nature.com/naturephotonics. Reprints and permission information is available online at http://www.nature.com/reprints. Correspondence and requests for materials should be addressed to S.K. and C.W.W.

nature photonics
SUPPLEMENTARY INFORMATION
DOI: 10.1038/NPHOTON.2011.129

Supplementary Information

I. Schematic representation of the zero-$\bar{n}$ superlattices

Schematic representation of a superlattice with 3 superperiods is shown in Fig. S1. The superlattice consists of alternating layers of hexagonal PhCs and homogeneous slabs. Note that the hexagonal PhC and the photonic superlattice have different symmetry properties, and therefore they also have different first Brillouin zones.

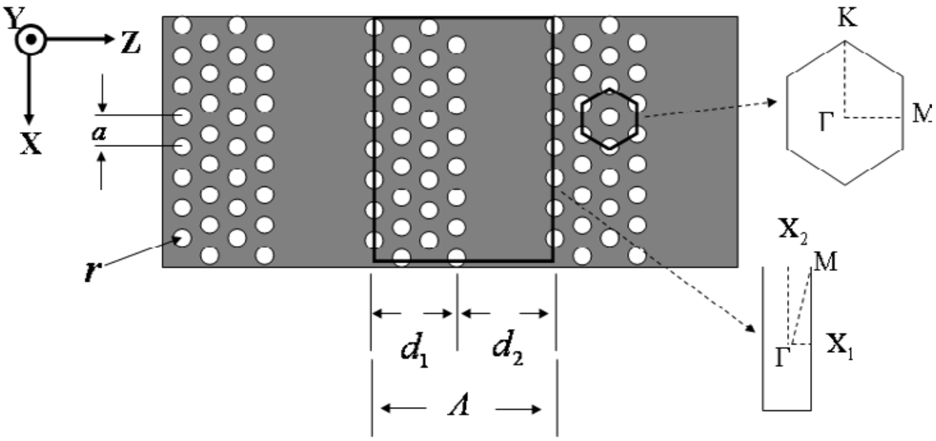

Figure S1 | Schematic representation of the photonic superlattice. There are two Brillouin zones defined as follows: one for the hexagonal photonic crystal lattice and one for the photonic superlattice. a is the lattice period and r is the radius of the holes forming the hexagonal lattice. d_1 is the length of the PhC layer and d_2 is the length of the PIM region. $d_1 + d_1 = \Lambda$ is equal to the superperiod (SP) of the photonic superlattice.

DOI: 10.1038/NPHOTON.2011.129

II. Effective indices from band diagram

The effective refractive indices corresponding to the TM-like bands (Fig. S2b) are determined from the relation $k=\omega|n|/c$ (with $\boldsymbol{k}$ in the first Brillouin zone) and plotted in Fig. S2c. Note that for the second band the effective index of refraction is negative since k decreases with ω [23].

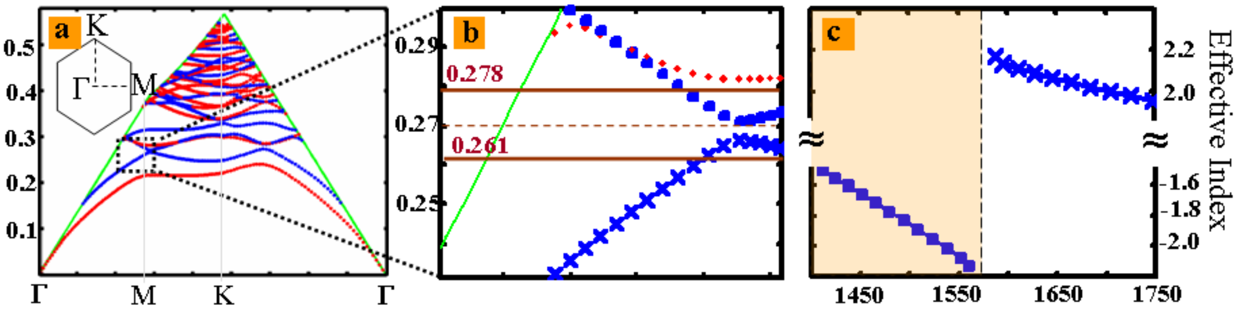

Figure S2 | Band diagram of the PhC, a, Band diagram of the PhC with the parameters given in Fig. 1. Inset: first Brillouin zone of the hexagonal PhC (for a schematic of the Brillouin zones, see the Supplementary Information, Fig. S1). The TM-like (TE-like) photonic bands are depicted in blue (red). The light cone is denoted by the green lines. **b,** A zoom-in of the spectral domain corresponding to experimental region of interest. Experiments were performed in the spectral region marked by the two horizontal lines (0.278-0.261 normalized frequency; 0.270 (dashed line) to 0.278 is negative index region). There is a complete TE-like band gap, and there are two TM-like bands. Lower frequency one band (marked with ×) has positive effective index of refraction, higher frequency band (marked with ■) has negative effective index of refraction. **c,** Calculated effective index of refraction of the PhC, corresponding to the two TM-like bands shown in Fig. S2b marked with the same symbols.

III. Device modification for phase measurements, and theoretical calculations for interferometer transmission

Figure S3 shows a schematic representation of a device with 2 superperiods and the integrated Mach Zehnder Interferometer is modified after introducing the third superperiod. The adiabatic region remains unchanged if L_1 is increased to $L_1+\Lambda$ and L_2 is shortened by $\Lambda/2$, in both the input and output sides of the device. To keep the total length of the waveguide unchanged, the length L_3 is increased to $L_3+\Lambda/2$. This procedure is used each time a superperiod is added to the structure. In addition, to be able to compare devices with different number of unit cells in the PhC layer, a common reference point is used for all devices that have the same d_2/d_1 ratio.

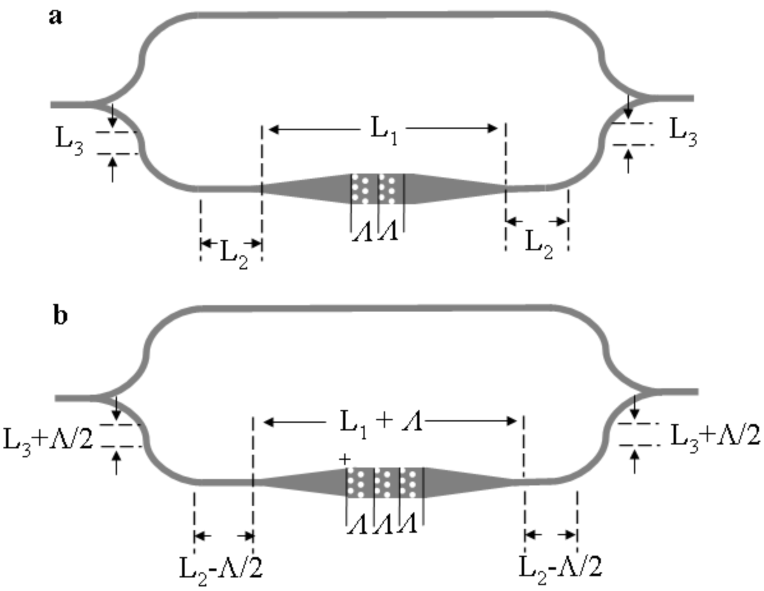

Figure S3| Schematic representation of the device modification induced by adding a superperiod. a, Integrated MZI of a device with 2 superperiods and a channel waveguide. **b,** Device modifications after the third superperiod is added. The length of the channel waveguide remains the same so as the effect of the additional superperiod is isolated.

In our implementation, the interferometer output intensity is given as:

$$I = I_1 + I_2 + 2\sqrt{I_1 I_2}\cos\phi \qquad \text{(S1)}$$

where ϕ is the phase difference (or imbalance) between the modes propagating in the two arms (denoted by subscript 1 and 2). Considering our implementation, the phase ϕ can be decomposed as:

$$\begin{aligned}\phi = \phi_1 - \phi_2 &= \frac{2\pi}{\lambda}\left[\left(n_{wg}L_{wg\_1} + n_{slab\_1}L_{slab\_1} + n_{sl}L_{sl}\right) - n_{wg}L_{wg\_2}\right] \\ &= \frac{2\pi}{\lambda}\left[n_{wg}\left(L_{wg\_1} - L_{wg\_2}\right) + n_{slab\_1}L_{slab\_1}\right] + \frac{2\pi}{\lambda}n_{sl}L_{sl}\end{aligned} \qquad \text{(S2)}$$

where n_{wg}, n_{slab_1}, n_{sl} are the effective mode refractive indices of the channel waveguide, the adiabatic slab in arm 1, and the zero-index superlattice, respectively. L_i denotes the corresponding lengths.

We note that the difference between the physical path length of the channel waveguides on both arms is designed to be equal to the physical path length of the tapering slab. Thus we have:

$$\begin{aligned}\cos[\phi] &= \cos\left[\frac{2\pi}{\lambda}\left(\left(-n_{wg}L_{Slab\_1} + n_{Slab\_1}L_{Slab\_1}\right) + n_{sl}L_{sl}\right)\right] \\ &= \cos\left[\frac{2\pi}{\lambda}\left(\left(n_{Slab\_1} - n_{wg}\right)L_{Slab\_1} + n_{sl}L_{sl}\right)\right] \\ &= \cos\left[\phi_{slab-wg} + \phi_{sl}\right]\end{aligned} \qquad \text{(S3)}$$

The mode indices n_{wg}, n_{slab_1}, n_{sl} have different frequency dispersion. We kept the phase (ϕ_{slab_wg}), arising from $\frac{2\pi}{\lambda}\left(n_{slab\_1} - n_{wg}\right)L_{slab\_1}$, constant between different devices in each set of measurements by simply ensuring that the physical lengths and widths of the slabs are the same for each nanofabricated device. The remaining phase variation therefore is generated only by the photonic crystal superlattice ($\phi_{sl} = \frac{2\pi}{\lambda}n_{sl}L_{sl}$). If n_{sl} is equal to zero, ϕ_{sl} is zero too, hence the total phase difference ϕ in the interferometer arises only from the ϕ_{slab_wg} component and is the same for all the devices in each set. Therefore, the sinusoidal oscillations in the transmission and the free spectral range are determined only by ϕ_{slab_wg}.

IV. Experiments on tunability of the zero-$\bar{n}$ region

In order to demonstrate the tunable character of the zero-$\bar{n}$ bandgaps, we performed transmission experiments on four sets of binary superlattices, with each set having different superlattice ratios: d_2/d_1=0.74 (Fig. S4a), d_2/d_1=0.76 (Fig. S4b), d_2/d_1=0.78 (Fig. S4d), and d_2/d_1=0.8 (Fig. S4e). In all our experiments the negative index PhC has the same parameters as those given in the main text. Note that there is a slight (~5%) change in r/a, which results in a small shift (<1%) in the spectrum. For example, Fig. 2c in the main text and Fig. S4d here correspond to the same design but there is about 10 nm (~0.6%) shift in the center of the zero-$\bar{n}$ region. However, all the experimental data in this section corresponds to the same chip, therefore the invariance of the gap for the geometrical changes and its tunability can be clearly observed.

As described in the main text, each set of photonic superlattices consists of three devices of different period Λ, with the negative index PhC layer in the superlattice spanning 7, 9, and 11 unit cells along the z-axis, so that the thickness of this layer is $d_1 = 3.5\sqrt{3}\,a$ (2.564 µm), $d_1 = 4.5\sqrt{3}\,a$ (3.297 µm), and $d_1 = 5.5\sqrt{3}\,a$ (4.029 µm), respectively. The corresponding thickness of the PIM layer is determined by requiring that the average index is zero [$\bar{n} = (n_1 d_1 + n_2 d_2)/\Lambda = 0$], while keeping the ratio d_2/d_1 unchanged for all devices in each set (see Table S1). Here, n_1 and n_2 are the effective mode indices in the PhC and homogeneous (PIM) layers, respectively, at the corresponding wavelength.

Table S1 | Calculated parameters of the devices in the Fig. S4 (units in μm).

Fig. S4a			
# of unit cells	d_1	d_2	Λ
7	2.56	1.90	4.46
9	3.30	2.44	5.74
11	4.03	2.98	7.01

Fig. S4b			
# of unit cells	d_1	d_2	Λ
7	2.56	1.95	4.51
9	3.30	2.51	5.80
11	4.03	3.06	7.09

Fig. S4d			
# of unit cells	d_1	d_2	Λ
7	2.56	2.00	4.56
9	3.30	2.57	5.87
11	4.03	3.14	7.17

Fig. S4e			
# of unit cells	d_1	d_2	Λ
7	2.56	2.05	4.62
9	3.30	2.64	5.93
11	4.03	3.22	7.25

For the three devices in each set, we designed 7 SPs for the devices with 7 unit cells of PhC and 5 SPs for those with 9 and 11 unit cells of PhC (these designs ensure a sufficient signal-to-noise ratio for the transmission measurements). In these experiments we have tested both the existence of the zero-$\bar{n}$ bandgap as well as its tunability. For the three devices belonging to each set, we observed the zero-$\bar{n}$ bandgap at the same frequency whereas the spectral locations of the other bandgaps were observed to shift with the frequency – this confirms the zero-$\bar{n}$ bandgap does not depend on the superperiod length Λ (the gap existence is dependent only on the condition of path-averaged zero index: $n_1d_1 + n_2d_2 = 0$) while the frequency of the regular 1D PhC Bragg bandgaps does depend on Λ. Our measurements show that the invariant, zero-$\bar{n}$, bandgap is located at 1525.5 ±1 nm, 1535.2 ±2 nm, 1546.3 ±1.5 nm, and 1556.5 ±2.5 nm, respectively (averaged over the three devices in each set). The slight red-shift with increasing number of unit cells in each set is due to effects of edge termination between the PhC and the homogeneous slab.

Furthermore, when we tuned the ratio d_2/d_1 and repeated these same experiments we observed a redshift (see the values above) of the zero-$\bar{n}$ mid-gap frequency as we increased the ratio d_2/d_1. This result is explained by the fact that for the negative index band the refractive index of the 2D hexagonal PhC decreases with respect to the wavelength (see Fig. S2c) and therefore when the length of the PIM layer in the 1D binary superlattice increases (higher d_2/d_1), the wavelength at which the effective index cancels is red-shifted. The effective index of the PIM layer, n_2, is calculated numerically and for the asymmetric TM slab waveguide mode corresponds to, for example, 2.671 at 1550 nm. By using these n_1 (Fig. S2c) and n_2 values, we determined the average refractive index for the different d_2/d_1 ratios as summarized in Fig. S4f. A distinctive red-shift in the zero-$\bar{n}$ gap location is observed with increasing d_2/d_1 ratios from the numerically modeling, demonstrating good agreement (~0.5% difference) with the experimental measurements (Fig. S4a, 4b, 4d, and 4e). Furthermore, Fig. S4c shows how the spectral features of the zero-$\bar{n}$ bandgap changes with increasing the number of superperiods. We note that this is the first rigorous and complete experimental confirmation of invariant and tunable character of zero-$\bar{n}$ bandgaps in photonic superlattices containing negative index PhCs.

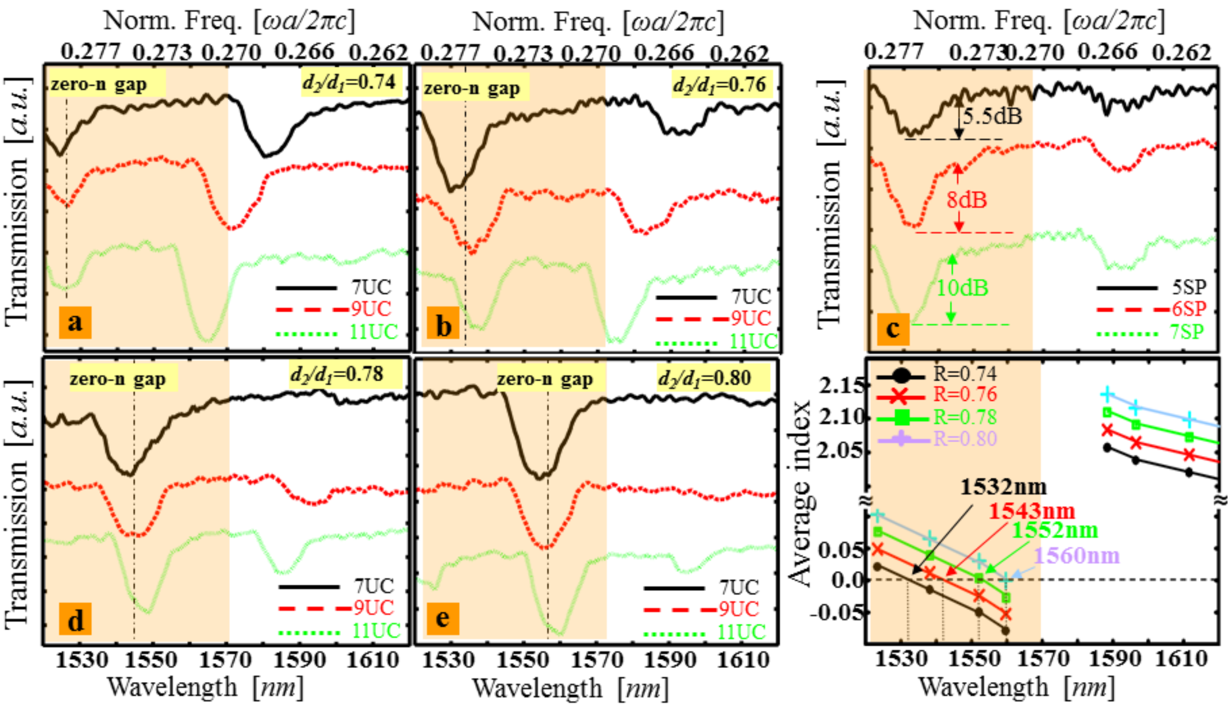

Figure S4 | Experimental verification of period-invariance and tunability of zero-$\bar{n}$ bandgaps. a, Experimental verification of the zero-$\bar{n}$ bandgap in superlattices with varying period (Λ). The ratio d_2/d_1 =0.74 and Λ=4.46 μm for black (solid), 5.74 μm for red (dashed), and 7.01 μm for green (dotted) curves (*a.u.* arbitrary units). **b,** Same as in **a**, but for d_2/d_1 =0.76. Λ=4.51 μm for black (solid), 5.80 μm for red (dashed), and 7.09 μm for green (dotted) curves. **c,** Transmission spectra for superlattices with d_2/d_1=0.76, containing 5, 6, and 7 superperiods (SPs). Each PhC layer contains 7 unit cells (d_1=2.564 μm, Λ=4.51μm). **d,** Same as in **a**, but for d_2/d_1=0.78. Λ=4.56 μm for black (solid), 5.87μm for red (dashed), and 7.17 μm for green (dotted) curves. **e,** Same as in **a**, but for d_2/d_1=0.80. Λ=4.62 μm for black (solid), 5.93 μm for red (dashed), and 7.25 μm for green (dotted) curves. **f,** Calculated effective index of refraction for the superlattices with the ratios in **a**, **b**, **d**, and **e**. The wavelengths at which the average index of refraction cancels agree very well with the measured values.

V. Near-field scanning optical microscopy and high-resolution imaging measurements

We further used near-field scanning optical microscopy (NSOM) to examine the zero-$\bar{n}$ transmission in the near-field, as illustrated in Fig. S5. Our NSOM is an aperture-type instrument, where the fiber is produced in National Chiao Tung University in Taiwan by using of thermal pulling method. A metal coating is used to create the aperture. The NSOM fiber was then attached to a tuning fork sensor produced by Veeco Instruments. The detection is performed with a New Focus 2153 InGaAs femtowatt photoreceiver with lock-in amplification. The NSOM instrument is a modified Veeco Aurora-3.

Coupling light into the zero-$\bar{n}$ superlattices is achieved by UV-curing adhesive bonding of a tapered lens fiber to the silicon input waveguide. The input fiber was stably UV-epoxy bonded to the devices selected for the measurements. We observed the light propagation through the sample by NSOM and used a widely tunable laser with controlled polarization to vary the input wavelength. From the near-field images of the superlattices (9 unit cells in PhC layer and d_2/d_1~0.76), it can be seen that the light propagation in the superlattices is characterized by low transmission inside the zero-$\bar{n}$ gap (Fig. S5a, λ=1535 nm), and high transmission outside the zero-$\bar{n}$ gap (Fig. S5b, λ= 1560 nm).

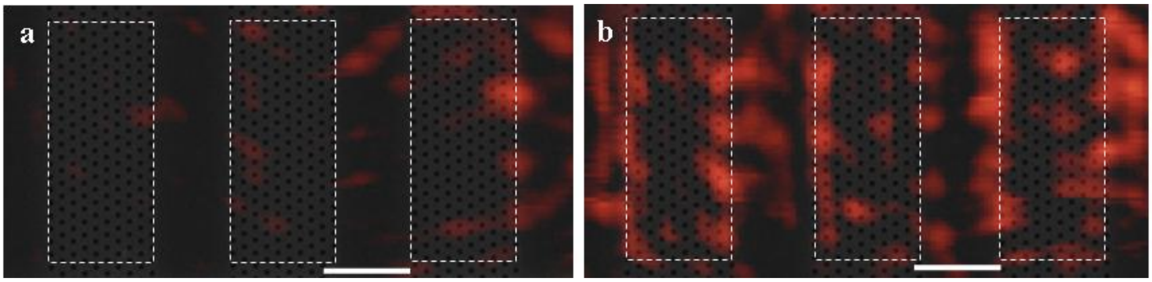

Figure S5| Near-field scanning optical microscopy of zero-$\bar{n}$ superlattices. a, Near-field image of a zero-$\bar{n}$ device that has 9 unit cells in each PhC layer at λ=1535 nm (in the center of

DOI: 10.1038/NPHOTON.2011.129

the gap). **b,** Same as in **a** at λ=1560 nm (in the high transmission). Scattering occurs at the edge of the PhC/PIM interfaces and is an indicative of transmission. Scale bar: 2.5 μm.

In addition, we performed high spatial resolution imaging of the radiated input-output ports for the devices that have been used for the experiment presented in Fig.3c. Results are illustrated in the Fig S6 as follow: In the case of the reference arm **(i-iii)**, we see light transmission for all three wavelengths, which corroborates the characteristics of the transmission spectrum in Fig. 3c. For the device arm (**iv-vi**) there is transmission for 1600 nm and 1530 nm but not for 1570 nm. This agrees with the transmission spectra in Fig. 3c. Note that although there is similar transmission for both arms at 1530 and 1600 nm, the interference output has 14dB difference.

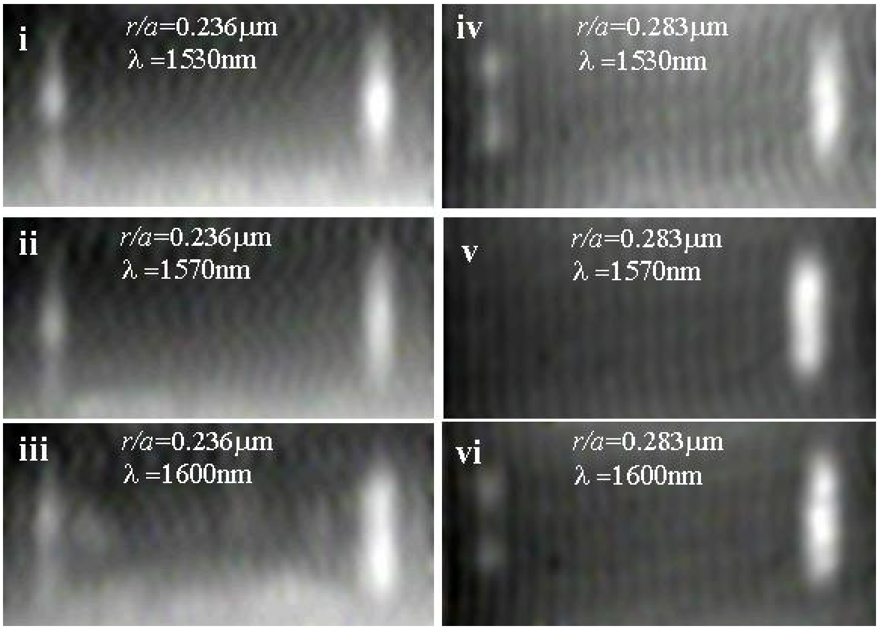

Figure S6| Infrared images pertaining to the experiments corresponding to Fig3c. i-iii is taken from the reference arm containing a PhC structure with *r/a*=0.236 and **iv-vi** is taken from the device arm where the ratio *r/a*=0.283. In all the images the input beam is impinging onto the structure from the right, which means that light scattering at the left facet of the device indicates light transmission.

VI. Computational study of the influence of disorder on the properties of zero-$\bar{n}$ superlattices.

In addition to the model for structural disorder of the photonic superlattice discussed in the paper, we have also considered two other disorder models in which either the radius of each hole in the PhC sections or the position of the holes is randomly perturbed. More exactly, the radius of the holes is set in the domain ($r-\Delta r/2$, $r+\Delta r/2$), according to a uniform random distribution whereas in the second case the location of the holes is randomly perturbed by Δl. In these models, the degree of structural disorder is characterized by a disorder parameter defined as $\sigma=\Delta r/r$ and $\sigma=\Delta l/a$, respectively. The main results of our computational investigations are summarized in Fig. S7. Thus, it can be seen that in the case of random perturbation of the radius of the holes the transmission spectra in the superlattice are only slightly affected, even if the disorder parameter is as large as $\sigma=10\%$. As observed, the main effect consists of a small decrease of the zero-$\bar{n}$ superlattice transmission with increasing values of the disorder parameter σ. It is seen, however, that structural disorder induced by randomly changing the location of the holes has a much larger effect on the transmission spectra. We note though that a value of $\sigma=10\%$ corresponds to variations of tens of nanometers of the location of the holes, variations which are much larger than those measured in our fabricated devices.

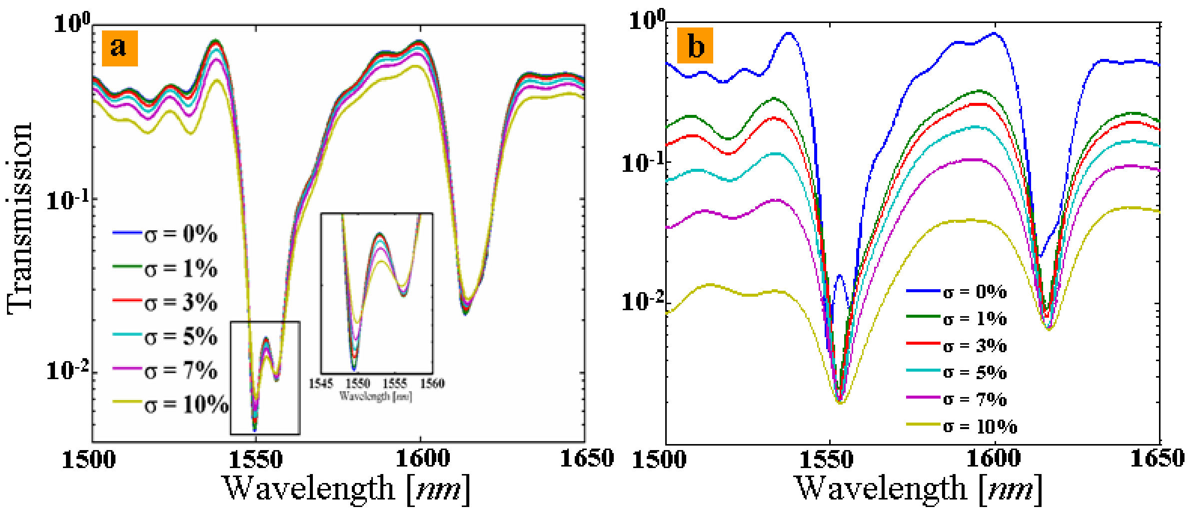

Figure S7 | Transmission spectra calculated for different values of the disorder parameter σ. The inset shows the expanded transmission spectra. **a**, The structural disorder is introduced by randomly changing the radius of the holes in the PhC sections of the superlattice. **b**, The structural disorder is generated by randomly perturbing the location of the holes.